WD40-repeat 47, a microtubule-associated protein, is essential for brain development and autophagy

Meghna Kannan[a,b,c,d,e,1], Efil Bayam[a,b,c,d,1], Christel Wagner[a,b,c,d], Bruno Rinaldi[f], Perrine F. Kretz[a,b,c,d], Peggy Tilly[a,b,c,d], Marna Roos[g], Lara McGillewie[h], Séverine Bär[f], Shilpi Minocha[e], Claire Chevalier[a,b,c,d], Chrystelle Po[i], Sanger Mouse Genetics Project[j,2], Jamel Chelly[a,b,c,d], Jean-Louis Mandel[a,b,c,d], Renato Borgatti[k], Amélie Piton[a,b,c,d], Craig Kinnear[h], Ben Loos[g], David J. Adams[j], Yann Hérault[a,b,c,d], Stephan C. Collins[a,b,c,d,l], Sylvie Friant[f], Juliette D. Godin[a,b,c,d], and Binnaz Yalcin[a,b,c,d,3]

[a]Department of Translational Medicine and Neurogenetics, Institut de Génétique et de Biologie Moléculaire et Cellulaire, 67404 Illkirch, France; [b]Centre National de la Recherche Scientifique, UMR7104, 67404 Illkirch, France; [c]Institut National de la Santé et de la Recherche Médicale, U964, 67404 Illkirch, France; [d]Université de Strasbourg, 67404 Illkirch, France; [e]Center for Integrative Genomics, University of Lausanne, CH-1015 Lausanne, Switzerland; [f]Génétique Moléculaire Génomique Microbiologie, UMR7156, Université de Strasbourg, CNRS, 67000 Strasbourg, France; [g]Department of Physiological Sciences, University of Stellenbosch, 7600 Stellenbosch, South Africa; [h]South African Medical Research Council Centre for Tuberculosis Research, Department of Biomedical Sciences, University of Stellenbosch, 7505 Tygerberg, South Africa; [i]ICube, UMR 7357, Fédération de Médecine Translationnelle, University of Strasbourg, 67085 Strasbourg, France; [j]Wellcome Trust Sanger Institute, Hinxton, CB10 1SA Cambridge, United Kingdom; [k]Neuropsychiatry and Neurorehabilitation Unit, Scientific Institute, Istituto di Ricovero e Cura a Carattere Scientifico Eugenio Medea, 23842 Bosisio Parini, Lecco, Italy; and [l]Centre des Sciences du Goût et de l'Alimentation, Université de Bourgogne-Franche Comté, 21000 Dijon, France

The family of WD40-repeat (WDR) proteins is one of the largest in eukaryotes, but little is known about their function in brain development. Among 26 WDR genes assessed, we found 7 displaying a major impact on neuronal morphology when inactivated in mice. Remarkably, all seven genes showed corpus callosum defects, including thicker (*Atg16l1*, *Coro1c*, *Dmxl2*, and *Herc1*), thinner (*Kif21b* and *Wdr89*), or absent corpus callosum (*Wdr47*), revealing a common role for WDR genes in brain connectivity. We focused on the poorly studied WDR47 protein sharing structural homology with LIS1, which causes lissencephaly. In a dosage-dependent manner, mice lacking *Wdr47* showed lethality, extensive fiber defects, microcephaly, thinner cortices, and sensory motor gating abnormalities. We showed that WDR47 shares functional characteristics with LIS1 and participates in key microtubule-mediated processes, including neural stem cell proliferation, radial migration, and growth cone dynamics. In absence of WDR47, the exhaustion of late cortical progenitors and the consequent decrease of neurogenesis together with the impaired survival of late-born neurons are likely yielding to the worsening of the microcephaly phenotype postnatally. Interestingly, the WDR47-specific C-terminal to LisH (CTLH) domain was associated with functions in autophagy described in mammals. Silencing WDR47 in hypothalamic GT1-7 neuronal cells and yeast models independently recapitulated these findings, showing conserved mechanisms. Finally, our data identified superior cervical ganglion-10 (SCG10) as an interacting partner of WDR47. Taken together, these results provide a starting point for studying the implications of WDR proteins in neuronal regulation of microtubules and autophagy.

WD40-repeat proteins | corpus callosum agenesis | microcephaly | neurogenesis | autophagy

The function of WD40-repeat (WDR)-containing proteins, one of the largest eukaryotic protein families, is largely unknown. Their importance is, however, evident based on their highly conserved repeating units from bacteria to mammals (1), commonly made of seven repetitive blades of 40 amino acids that end with a tryptophan-aspartic acid dipeptide at the C terminus.

As shown by crystallography studies, including the crystal structure of the beta gamma dimer of the G-protein transducin (2), a classical WDR protein, all WDR proteins are predicted to fold into a circularized beta-propeller structure, serving as a rigid platform (or scaffold) for protein–protein interactions by providing many stable and symmetrical surfaces (3, 4). One reason why WDR domains may have been less studied than other common domains, such as kinases or PDZ or SH3 domains (3), is that no WDR domain has yet been found with catalytic activity (3), but

this does not mean that the scaffold domains are less important. To the contrary, their serving as a platform for multiple enzymatic reactions and signaling events is highly significant (5).

In recent years, human genetic studies have also begun to recognize the importance of WDR genes. Among 286 WDR genes annotated across both human and mouse genomes, mutations in 27 WDR genes (9.4%) have so far been implicated in brain disorders, notably in intellectual disability associated with malformations pertaining to anomalies of the corpus callosum (Dataset S1). Among these, *PAFAH1B1* [also known as LIS1, a WDR protein

Significance

We present an identification of the relevance of WD40-repeat (WDR) genes in brain connectivity, highlighting the power of unbiased mouse studies in the field of neuroscience. We focus on the poorly studied WDR47 protein sharing structural homology with LIS1, which causes lissencephaly. WDR47 plays a role in progenitor proliferation, neuronal migration, and fiber tract projections in a similar fashion to LIS1 but with the distinctive particularity that WDR47 inhibits autophagic flux. This provides a functional link between autophagy biology and the C-terminal to LisH domain in mammals. Importantly, WDR47 uncovers an aspect of corpus callosum biology pointing toward a link between the regulation of microtubule dynamics and autophagic flux for axonal outgrowth and guidance.

identified 20 y ago to regulate dynein activity and neuronal migration (6)] is linked with lissencephaly type 1, a severe malformation where the brain develops without convolutions (Online Mendelian Inheritance in Man 607432), and the corpus callosum is thinner (7). Mutations in *WDR62* cause autosomal recessive primary microcephaly and hypoplasia of the corpus callosum (8), and *WDR73* is implicated in Galloway–Mowat syndrome characterized by microcephaly and thin corpus callosum (9). Understanding the underlying pathophysiological mechanisms of callosal disorders is critical for patient stratification and therapy development.

Made of ~190 million axonal projections, the human corpus callosum is the largest interhemispheric white matter tract in the brain, with neurons located mainly in neocortical layers II/III, giving rise to callosal axons (10). The genetics of corpus callosum biology is, however, highly heterogeneous, and despite technological advances in next generation sequencing, 75% of callosal disorders have no identified genetic cause (11). Recent studies have suggested that a smaller corpus callosum is associated with a higher risk for autisms (12), bipolar disorder (13), and schizophrenia (14). Corpus callosum abnormalities are often seen in conjunction with other defects, such as smaller or larger brain size and malformations of cortical development (15). The formation of the corpus callosum is a process relying on axonal guidance cues, such as Netrin/DCC, ROBO, and Slit (16). This developmental process also relies on microtubule polymers that localize to the tip of the axon, known as the growth cone (17). However, much less is known about microtubules at the growth cone, but they are the primary effectors of axonal movement and guidance (18).

Less than 3% of WDR proteins have been functionally defined in the CNS, while for the remaining 97%, the function remains completely unknown (Dataset S1). Interestingly, several WDR proteins have been linked to microtubules in KO mouse studies [for example, LIS1 (19) and WDR62 (20)]. Microtubules are critical components of the cytoskeleton, and their dynamics refers to the continuous remodeling between assembly (rescue) and disassembly (catastrophe) at their tip (21). Proper regulation of this dynamic is essential and achieved through microtubule-associated proteins.

In this study, we ask whether microtubule-mediated processes might be affected by mutations of WDR genes that result in corpus callosum anomalies, what the underlying cellular and molecular mechanisms are, and ultimately, how these underlie corpus callosum biology.

Results

Mouse WDR Proteins Are Implicated in Corpus Callosum Biology. Twenty-six WDR domain-containing mouse mutants were randomly selected among a manually curated list of 286 family members (Dataset S1) and studied at 16 wk of age. We first carried out gene ontology enrichment analysis in both 286- and 26-gene sets and found the same three most significant terms ($P < 0.001$): protein complex binding, actin filament binding, and histone binding (Fig. S1A).

Using a quantification approach of 66 morphological and 115 cellular measurements across 19 different brain regions in two histological sections at Bregma +0.98 mm and −1.34 mm (Datasets S2 and S3), we found that mutations of seven WDR genes ($Atg16l1^{+/-}$, $Coro1c^{+/-}$, $Dmxl2^{+/-}$, $Herc1^{-/-}$, $Kif21b^{-/-}$, $Wdr47^{-/-}$, and $Wdr89^{-/-}$) were associated with neuroanatomical phenotypes (Fig. 1; Datasets S4 and S5 show *P* values and percentage changes). At the morphological level, $Dmxl2^{+/-}$ and $Herc1^{-/-}$ displayed macrocephaly, with increased sizes of 37% ($P = 0.0005$) and 20% ($P = 0.002$), respectively. By contrast, $Wdr47^{-/-}$ and $Kif21b^{-/-}$ revealed microcephaly, with decreases in size of 25% ($P = 0.03$) and 20% ($P = 0.05$), respectively. $Atg16l1^{+/-}$ was associated with increased height (+11%) of the motor cortex ($P = 0.003$) and increased height (+38%) of the radiatum layer of the hippocampus ($P = 0.004$), whereas $Wdr89^{-/-}$ and $Coro1c^{+/-}$ were associated with ventricular atrophy (−13%) of the dorsal third ventricle ($P = 0.0009$)
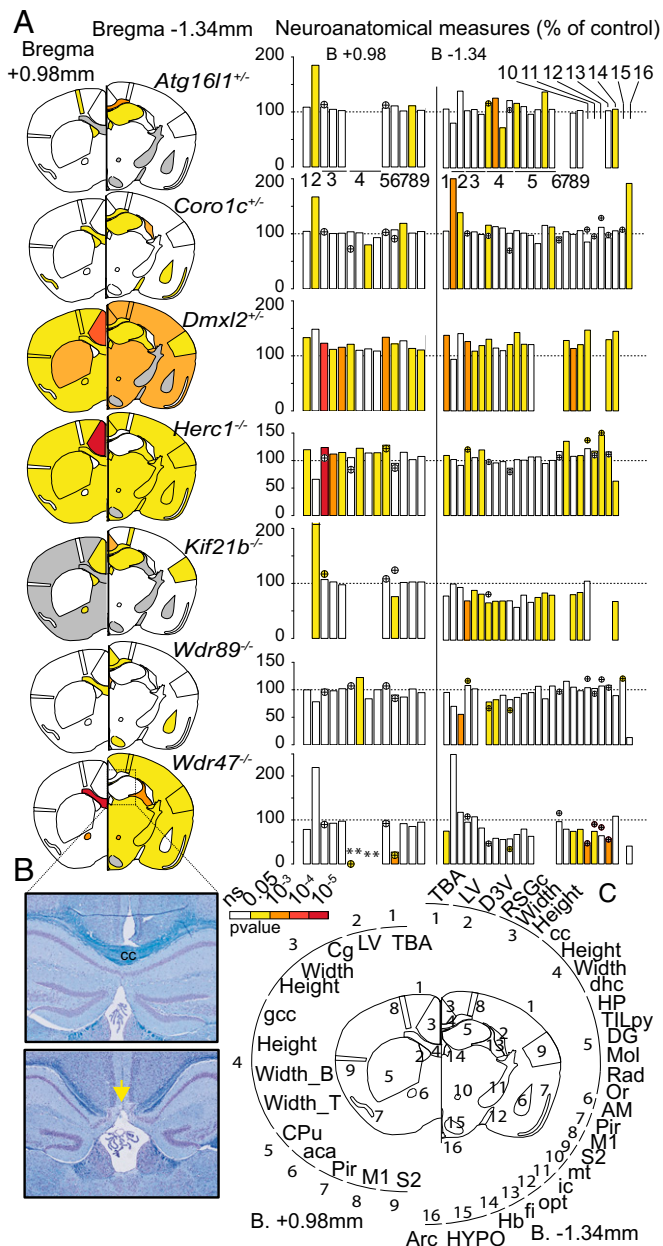

Fig. 1. Relevance of mouse WDR genes in adult brain morphogenesis. (*A*) Brain features plotted in two coronal planes according to *P* values for seven WDR genes (*n* = 3 per group). White indicates *P* > 0.05, and gray indicates no data. Histograms of percentage changes relative to WT animals (100%) are colored according to the significance level. Circles with crosses indicate cell count measurements. Statistical analyses were carried out using the linear mixed model framework within Phenstat (56). *Agenesis of the assessed region. (*B*) Brain images at Bregma −1.34 mm stained with cresyl violet and luxol blue showing the corpus callosum (cc) in WT (*Upper*) and agenesis of the cc in $Wdr47^{-/-}$ (*Lower*). The yellow arrow shows the agenesis (absence) of the corpus callosum. (Magnification: 20×.) (*C*) Numbers around the circle show assessed brain regions (a description is provided in Dataset S2). aca, anterior part of anterior commissure; AM, amygdala; Arc, arcuate nucleus; B, bottom; Cg, cingulate cortex; CPu, caudate putamen; D3V, dorsal third ventricle; DG, dentate gyrus; dhc, dorsal hippocampal commissure; fi, fimbria; gcc, genu of cc; Hb, habenula; HP, hippocampus; HYPO, hypothalamus; ic, internal capsule; LV, lateral ventricles; M1, motor cortex; Mol, molecular layer of HP; mt, mammillothalamic tract; ns, not significant; opt, optical nerve; Or, oriens layer of HP; Pir, piriform cortex; Rad, radiatum layer of HP; RSGc, retrosplenial granular cortex; S2, somatosensory cortex; T, top; TBA, total brain area; TILpy, total pyramidal cell layer.

and an enlargement (+13%) of the lateral ventricles ($P = 0.0002$), respectively. At the cellular level, $Herc1^{-/-}$ displayed a 37% increase in cell numbers in the mammillothalamic tract ($P = 0.003$) and a 20% increase in the granular cortex ($P = 0.001$), while $Kif21b^{-/-}$ showed a decreased number of cells (-17%) in the cingulate cortex ($P = 0.03$).

All seven WDR mutants displayed corpus callosum anomalies (Fig. 1*A* and Datasets S4 and S5). Developmental mechanisms regulating the dorsoventral axes of the corpus callosum being distinctive, with pioneering axons projecting from the cingulate cortex crossing the dorsal region and neurons from the neocortex regulating formation of the ventral region (22), we quantified several regions of the corpus callosum (the genu, soma, and splenium). $Dmxl2^{+/-}$ and $Herc1^{-/-}$ strongly impacted the genu, while $Atg16l1^{+/-}$, $Coro1c^{+/-}$, $Kif21b^{-/-}$, and $Wdr89^{-/-}$ affected the soma only. In addition, $Atg16l1^{+/-}$, $Coro1c^{+/-}$, $Wdr37^{-/-}$, and $Wdr89^{-/-}$ exhibited cell count defects in the corpus callosum, the directionalities of which were in line with those of the morphological phenotypes. $Wdr47^{-/-}$ stood out as the most severely affected gene, with agenesis of the corpus callosum (Fig. 1*B*), defined as a failure to develop the large bundle of fibers that connect the cerebral hemispheres (11).

Wdr47 Is Highly Expressed in the Adult Brain and Is Essential for Survival in Mice. We chose to focus on the poorly studied WDR47 gene (23) given the severity of the associated neuroanatomical phenotypes and developed two mouse models (tm1a and tm1b) (*Materials and Methods* and Fig. S1*B*). We validated both models using qRT-PCR and determined that tm1a is a hypomorph allele in a series of tissues, suggesting that *Wdr47* is skipping over the LacZ cassette restoring gene expression, while tm1b is a complete loss-of-function (LoF) of *Wdr47* (Fig. 2*A*). Based on average relative expression to the WT, tm1a heterozygous (het) mice, hereafter referred as $Wdr47^{+/tm1a}$, expressed 70%, and tm1b het $Wdr47^{+/tm1b}$ expressed 50% (Dataset S6). In homozygous (hom) animals, tm1a ($Wdr47^{tm1a/tm1a}$) and tm1b ($Wdr47^{tm1b/tm1b}$) expressed 30 and 0%, respectively (Dataset S6), offering the opportunity to study the impact of gene dosage (70, 50, and 30%) and complete gene LoF. WDR47 protein analysis confirmed minimal expression in $Wdr47^{tm1a/tm1a}$ (Fig. 2*B*). LacZ spatial expression throughout the brain and in peripheral tissues revealed *Wdr47* expression mainly in layers II/III of the cortex, pyramidal cells of the hippocampus, spinal cord, ventromedial hypothalamus, and arcuate nucleus (Fig. 2*C*). *Wdr47* was less expressed in peripheral tissues (Fig. 2*A* and Fig. S1*C*).

Adult mouse survival was assessed from 1,085 successfully genotyped mice derived from a heterozygous-by-heterozygous ("het-by-het") breeding scheme (Dataset S7); 5.7% hom, 54.2% het, and 40.1% WT were obtained in $Wdr47^{tm1a}$, and 0% hom, 55% het, and 45% WT were obtained in $Wdr47^{tm1b}$, indicating lethality in both het and hom mice. *Wdr47* expression levels and lethality (expressed as percentages) exhibited a high negative correlation (Fig. 2*D*), with males and females being equally affected. To determine the window of death, we then tested mouse viability from embryonic d 9.5 (E9.5) to 153 d of age (P153) (Fig. 2*E*). Death rate was unaffected during embryogenesis, and no abnormality in number of somites, limb morphology, and heartbeat was observed in E9.5 embryos ($n = 34$) and E18.5 $Wdr47^{tm1a/tm1a}$ embryos ($n = 132$). However, the percentage of $Wdr47^{tm1a/tm1a}$ decreased exponentially from birth to P55, with a reduction of 36% by P16 and a further reduction of 64% by P55. Mice that survived until P55 survived until adulthood. The cause of lethality remains unknown; however, histological assessment at E18.5 excluded lung defects.

It has been recently reported that a lipid-enriched diet rescues lethality in a mouse model of amyotrophic lateral sclerosis (24). We thus maintained a separate colony of mice on a fortified diet (Mouse Breeder Diet 5021) with extra lipids (10.8% as opposed to 3% in a normal diet) and folic acid (3 vs. 0.7 mg) using a het-by-
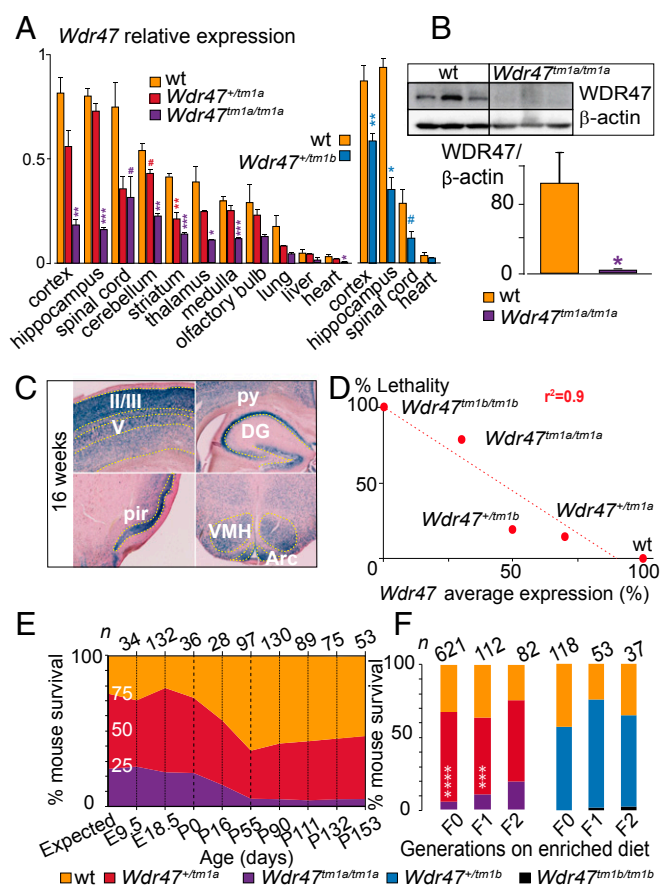

Fig. 2. Characterization of *Wdr47* mouse models. (*A*) *Wdr47* relative expression using qRT-PCR in $Wdr47^{+/tm1a}$ ($n = 3$), $Wdr47^{tm1a/tm1a}$ ($n = 3$), and WT ($n = 3$) across 11 tissues and in $Wdr47^{+/tm1b}$ ($n = 3$) and WT ($n = 3$) across 4 tissues (cortex, hippocampus, spinal cord, and heart). Normalization was done using GNAS (guanine nucleotide-binding protein, alpha-stimulating). (*B*) WDR47 protein profiling in cortex of WT ($n = 3$) and $Wdr47^{tm1a/tm1a}$ ($n = 3$). Normalization was done using β-actin. (*C*) LacZ staining in adult $Wdr47^{+/tm1a}$ across the cortex, pyramidal cells (py), dendate gyrus (DG), piriform cortex (pir), arcuate nucleus (Arc), and ventromedial part (VMH) of the hypothalamus. (Magnification: 20×.) (*D*) Correlation between *Wdr47* average expression and percentage mouse lethality; 843 $Wdr47^{tm1a}$ and 242 $Wdr47^{tm1b}$ were used. A linear regression was fitted ($r^2 = 0.9$). (*E*) Mouse survival outcome carried out at nine time points both in $Wdr47^{tm1a}$ males and in $Wdr47^{tm1a}$ females. Expected ratio indicates 25% for WT, 50% for $Wdr47^{+/tm1a}$, and 25% for $Wdr47^{tm1a/tm1a}$. (*F*) Mouse survival outcome on supplementation in fortified diet with extra lipids and folic acid (3 vs. 0.7 mg) in $Wdr47^{tm1a}$ and $Wdr47^{tm1b}$ across three generations. Plots are represented as mean + SEM. Statistical analysis was done using Student's *t* test (two-tailed; *A* and *B*) and χ^2 test relative to expected counts (*F*). *$P < 0.05$; **$P < 0.01$; ***$P < 0.001$; ****$P < $ 1E-06; #$P < 0.07$.

het breeding scheme and examined its effects on 591 mice in both $Wdr47^{tm1a}$ and $Wdr47^{tm1b}$ (Fig. 2*F*). Remarkably, we found an almost complete transgenerational rescue of the lethal phenotype at the second generation in $Wdr47^{tm1a}$ mice. These results indicate that diet enrichment counterbalances the lethality effect, possibly by altering nutrient levels necessary in key processes for survival. There was no rescue in $Wdr47^{tm1b}$, suggesting that residual *Wdr47* expression is necessary for diet-induced survival reversal.

Wdr47 Deficiency Results in Severe Microcephaly and Fiber Tract Hypoplasia in Adult Male and Female Mice. Sexual dimorphism was assessed through a newly designed sagittal analysis of 95 variables for 22 unique brain regions across three selected sections (lateral 0.72, 1.32, and 2.52 mm) (Fig. S2). This analysis had
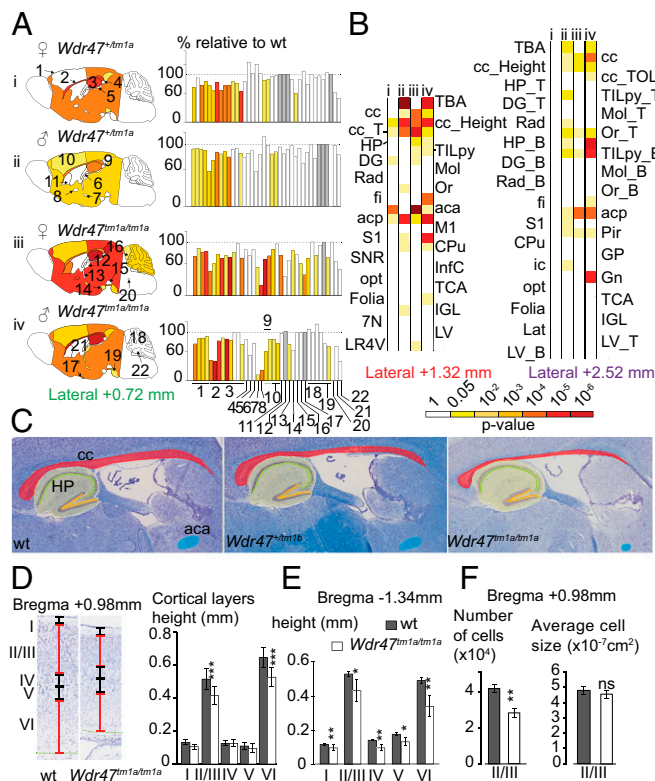
Fig. 3. Major fiber tracts defects and microcephaly in adult male and female mice. (*A*) Heat map of 22 brain regions quantified at lateral 0.72 mm (Fig. S2*B* and Dataset S8) across *Wdr47*^+/tm1a^ and *Wdr47*^tm1a/tm1a^, both male and female, vs. respective WT (*n* = 3 in each group). Histograms of percentage changes in comparison with WT (100%). (*B*) Heat map of 25 and 31 sagittal brain regions quantified at lateral 1.32 mm and 2.52 mm in male and female *Wdr47*^+/tm1a^ and *Wdr47*^tm1a/tm1a^, respectively. (*C*) Sagittal sections stained with cresyl violet and luxol blue in mice with reducing relative expression of Wdr47. (Magnification: 20×.) (*D*) Height of cortical layers in adult *Wdr47*^tm1a/tm1a^ (*n* = 6) compared with WT (*n* = 6) at Bregma +0.98 mm. (*E*) Height of cortical layers at Bregma −1.34 mm in *Wdr47*^tm1a/tm1a^ compared with WT. (*F*) Number of cells and cell sizes in layers II/III in *Wdr47*^tm1a/tm1a^ (*n* = 6) compared with WT (*n* = 6). Plots are represented as mean + SEM. *P < 0.05 (Student's *t* test, two-tailed); **P < 0.01 (Student's *t* test, two-tailed); ***P < 0.001 (Student's *t* test, two-tailed). 7N, facial nucleus; aca, anterior part of anterior commissure; acp, posterior part of anterior commissure; B, bottom; cc, corpus callosum; CPu, caudate putamen; DG, dentate gyrus; fi, fimbria; Gn, geniculate nucleus; GP, globus pallidus; HP, hippocampus; ic, internal capsule; IGL, internal granule cell layer; InfC, inferior colliculus; Lat, lateral cerebellar nucleus; LR4V, fourth ventricle; LV, lateral ventricles; M1, motor cortex; Mol, molecular layer of HP; ns, not significant; opt, optical nerve; Or, oriens layer of HP; Pir, piriform cortex; Rad, radiatum layer of HP; S2, somatosensory cortex; SNR, substantia nigra; T, top; TBA, total brain area; TCA, total cerebellar area; TILpy, total pyramidal cell layer.

the advantage of adding new brain regions (such as the substantia nigra) while maintaining existing ones in 16-wk-old *Wdr47*^+/tm1a^ and *Wdr47*^tm1a/tm1a^ (Datasets S8 and S9). Consistently, male and female *Wdr47*^tm1a/tm1a^ showed a similar set of neuroanatomical anomalies (for example, at lateral 0.72 mm), a reduction in the total brain area of 27.5% for female (*P* = 0.014) and 25.1% (*P* = 0.0015) for male, a decrease in the area of the corpus callosum of 54.9% (*P* = 0.027) for female and 54.8% (*P* = 0.046) for male, and a smaller anterior commissure area of 80.9% (*P* = 0.0007) for female and 75.2% (*P* = 0.004) for male (Fig. 3*A*). Conservatively, these results were recapitulated at lateral 1.32 and 2.52 mm, and *Wdr47*^+/tm1a^ showed similarities in neuroanatomical phenotypes but to a lesser extent than *Wdr47*^tm1a/tm1a^ (Fig. 3 *A* and *B* and Fig. S3*A*). Interestingly, we found a strong correlation between *Wdr47* relative expression and severity of brain structural anomalies, such

as in the corpus callosum and anterior commissure (Fig. 3*C*), both in male and female, showing that the role of *Wdr47* in brain morphogenesis is highly sensitive to dosage (Fig. S3*B*).

Next, we asked whether adult *Wdr47* KO mice bred on an enriched diet would show reversal of neuroanatomical defects, since folic acid diet supplementation can promote neuronal proliferation and reduce apoptosis (25). For this purpose, we used the same set of 181 parameters as our original analysis of coronal sections (Dataset S2), assessed 16-wk-old *Wdr47*^tm1a/tm1a^ mice derived from the second generation bred with fortified diet as well as from the chow diet colony, and compared them with their respective WTs. Similar neuroanatomical defects were identified in fortified mice compared with chow diet mice (Fig. S4), suggesting no amelioration aside from viability tests. Accordingly, additional tests on cortical layers revealed similar decrease in the height of layers II/III (−19.4%, *P* = 0.00007) and VI (−18.5%, *P* = 0.00036) at Bregma +0.98 mm (Fig. 3*D*) and reduction of all layers at Bregma −1.34 mm (Fig. 3*E*) in both diets. Focusing on layers II/III, where neurons giving rise to callosal axons originate (10), we found a 22.2% reduction in cell number (*P* = 0.00057) in both groups (Fig. 3*F*).

Wdr47 Mice Show an Embryonic Brain Size Phenotype That Worsens at Postnatal Stages.
To discriminate primary microcephaly (defined as reduction in brain size at birth) from acquired microcephaly (when brain size is normal at birth but reduces subsequently), we studied brain morphology at E18.5 using a quantification approach of 67 measurements of size and surface (Datasets S8 and S9) across three coronal planes at stereotactic position Bregma 2.19, 3.51, and 6.75 mm (Fig. S5).

In *Wdr47*^tm1a/tm1a^, 14 phenotypes emerged as decreased, including corpus callosum area at Bregma 2.19 mm (−23.3%, *P* = 0.0056) and motor cortex (−14.1%, *P* = 0.013 and −9%, *P* = 0.024 at Bregma 2.19 and 3.51 mm, respectively) (Fig. 4*A*). While the total brain area was not significantly affected across the three coronal planes, it showed a clear tendency toward reductions of size of 10.3% (*P* = 0.26), 10% (*P* = 0.06), and 7.1% (*P* = 0.31) at Bregma 2.19, 3.51, and 6.75 mm, respectively (Dataset S9). Similar phenotypes emerged in *Wdr47*^+/tm1a^, with fewer regions affected and smaller percentage changes compared with *Wdr47*^tm1a/tm1a^ (Fig. 4*A* and Dataset S9). To further investigate the reduction of the cortical thickness, we measured individual layers and found a reduction originating specifically from the cortical plate and sub- and ventricular zones at Bregma 2.19 mm (Fig. 4*B*).

Additionally, we measured 63 parameters in *Wdr47*^+/tm1a^ and *Wdr47*^tm1a/tm1a^ at P8 and found a similar set of regions being affected compared with in 16-wk-old mice (Fig. S6*A* and Dataset S9); in particular, the total brain area was reduced by 21.6% (*P* = 0.046), and the corpus callosum area was smaller by 55.6% (*P* = 0.033). We also analyzed mice at 56 wk of age and found that the brain size phenotypes did not worsen (Fig. S6 *B* and *C*). In summary, *Wdr47*^tm1a/tm1a^ mice exhibited reductions of the total brain size of 9, 22, 26, and 29% at E18.5, P8, 16 wk of age, and 56 wk of age, respectively, pointing toward primary microcephaly that worsens postnatally.

Wdr47 Regulates Progenitor Proliferation and Survival of Neurons in Late Corticogenesis.
Wdr47 cortical expression, assessed using Western blot analysis, gradually increased from E12.5 to P2, reaching a peak at E18.5 (Fig. 4*C*). Accordingly, LacZ spatiotemporal expression revealed an enriched *Wdr47* expression in layers II/III as corticogenesis progresses (Fig. 4*D*), suggesting a role of WDR47 in late corticogenesis.

The reduction of the thickness of the cortical plate at E18.5 (Fig. 4*B*) could arise from a poor survival of progenitors or neurons. In agreement with this hypothesis, *Wdr47*^tm1b/tm1b^ showed an increased level of apoptosis, mainly in upper-layer neurons (Fig. 4*E*), indicating that WDR47 is not required for the survival of the
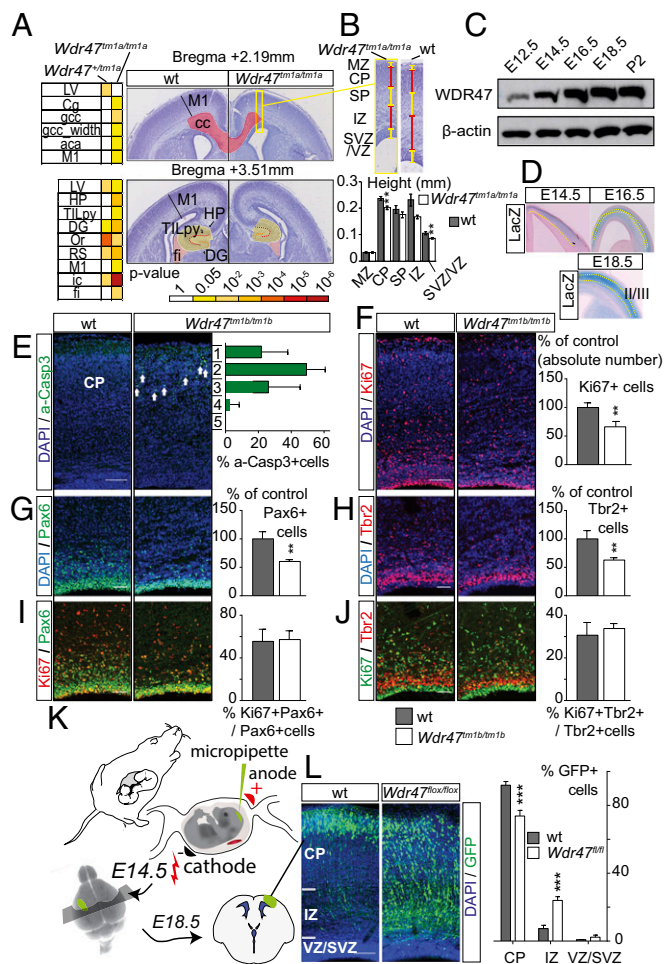
Fig. 4. Wdr47 is a key regulator in multiple steps of the neurogenic program. (*A*) Heat map of neuroanatomical defects in *Wdr47*[tm1a] at E18.5 (*n* = 4 *Wdr47*[tm1a/tm1a], *n* = 5 *Wdr47*[+/tm1a], *n* = 5 WT) (Dataset S9) and images illustrating neuroanatomical anomalies. (Magnification: 20×.) (*B, Upper*) Zoom in of boxed area in *A* showing height of neocortical layers in sections stained with cresyl violet from WT (*n* = 5) and *Wdr47*[tm1a/tm1a] (*n* = 4) embryos at E18.5. (*B, Lower*) Quantification of individual cortical layers. **$P < 0.01$ (Student's *t* test, two-tailed). (*C*) Western blot of WDR47 expression in WT cortical tissues from E12.5 to P2. β-actin is used as a loading control. (*D*) LacZ expression pattern in E14.5 to E18.5 *Wdr47*[+/tm1a] across the cortex (*n* = 3 per group). (*E*) Percentage of apoptotic cells in each bin of cortical plate from E18.5 WT (*n* = 3) and *Wdr47*[tm1b/tm1b] (*n* = 3) cortices [activated caspase 3+ (a-Casp3) in green]. Arrows point to a-Casp3+ cells. (*F*) E18.5 WT (*n* = 4) and *Wdr47*[tm1b/tm1b] (*n* = 4) cortices showing cycling progenitors (Ki67+ in red). (*G* and *H*) E18.5 WT (*n* = 3) and *Wdr47*[tm1b/tm1b] (*n* = 3) cortices showing apical progenitors (APs; Pax6+ in green) and intermediate progenitors (IPs; Tbr2+ in red). (*I* and *J*) E18.5 WT (*n* = 3) and *Wdr47*[tm1b/tm1b] (*n* = 3) cortices showing cycling APs (Pax6+ in green and Ki67+ in red) and cycling IPs (Tbr2+ in red and Ki67+ in green). **$P < 0.01$ (Student's *t* test, two-tailed). (*K*) In utero electroporation procedure. (*L*) E18.5 WT (*n* = 3) and *Wdr47*[flox/flox] (*n* = 3) cortices electroporated at E14.5 with NeuroD:Cre-GFP. The percentage of GFP+ cells represents neurons from the region highlighted in *L*. Plots are represented as mean + SEM. Images are produced using confocal microscopy, and nuclei counterstaining are performed with DAPI (blue). *Wdr47*[tm1b/tm1b] is expressed as proportion of control (*F*–*H*). aca, anterior part of anterior commissure; cc, corpus callosum; Cg, cingulate cortex; CP, cortical plate; DG, dentate gyrus; fi, fimbria; HP, hippocampus; ic, internal capsule; IZ, intermediate zone; LV, lateral ventricles; M1, motor cortex; MZ, marginal zone; Or, oriens layer; RS, retrosplenial granular cortex; SP, subplate; SVZ, subventricular zone; TIlpy, total pyramidal cell layer; VZ, ventricular zone. (Scale bars: *E, F,* and *L*, 100 μm; *G–J*, 50 μm.) ***$P < 0.0001$ (two-way ANOVA followed by Bonferroni correction).

earliest born neurons. Consistently, no cell death was observed at E16.5 (Fig. S7*A*). We next tested whether the primary microcephaly phenotype could also stem from an impaired generation of neurons in *Wdr47*[tm1b/tm1b] embryos. Using immunolabeling, we analyzed cortical progenitors in *Wdr47*[tm1b/tm1b] and WT E18.5 embryos and found a reduced number of Ki67+ cycling progenitors (−33.8%, $P = 0.0016$) (Fig. 4*F*) and a decrease in the absolute number of both Pax6+ apical (−39.7%, $P = 0.0064$) and Tbr2+ intermediate (−37.2%, $P = 0.0042$) progenitors (Fig. 4*H*). Noteworthy, the proliferative potential of both progenitor types remained unchanged (Fig. 4 *I* and *J*).

To understand the loss of progenitor cells at E18.5, we repeated our experiments at an earlier stage. *Wdr47*[tm1b/tm1b] E16.5 Pax6+ apical and Tbr2+ intermediate progenitors behaved as WT, with no observable phenotype in their absolute number (Fig. S7 *C* and *D*) or proliferative potential (Fig. S7 *E* and *F*). However, we observed a milder decrease in the number of Ki67+ cycling progenitors by 17% ($P = 0.018$) (Fig. S7*B*) compared with −33.8% at E18.5 (Fig. 4*F*). In addition, we assessed cell cycle exit and fate of newborn cells by injecting 5-ethynyl-2-deoxyuridine (EdU) at E15.5 and studying corresponding *Wdr47*[tm1b/tm1b] embryos 24 h later at E16.5. We found no differences in the fate of newborn Pax6+ and Tbr2+ progenitors (Fig. S7 *G* and *H*) but a slight increase in the number of progenitors that exited the cell cycle (+10.7%, $P = 0.027$) (Fig. S7*I*) together with decreased proliferation (Fig. S7*B*), suggesting that the reduction of progenitors self-renewal starts from E16.5 onward and progressively increases until E18.5.

Specific Deletion of Wdr47 in Postmitotic Neurons Impairs Radial Migration. Given that WDR47 is involved in the neurogenic program and has been identified as a microtubule-associated protein (23), we tested whether, in addition to neurogenesis, WDR47 could also regulate neuronal migration. We performed acute deletion of WDR47 in projection neurons by in utero electroporation of plasmids, allowing the expression of the CRE recombinase and the GFP under the control of the NeuroD promotor (NeuroD:CRE-GFP) at E14.5 (Fig. 4*K*). Four days after in utero electroporation, while most of the GFP+ postmitotic neurons reached the cortical plate in the control (Fig. 4*L*), neurons depleted for WDR47 (NeuroD:CRE-GFP in WDR47^{fl/fl} embryos) accumulated in the intermediate zone, with a decrease of 20% of the cells reaching the cortical plate (Bonferroni adjusted $P = 0.0001$) (Fig. 4*L*). The role of WDR47 in radial migration of projection neurons was confirmed in KO mice, as we observed similar positioning defects of EdU-labeled cells 4 d after a single EdU injection in E14.5 *Wdr47*[tm1b/tm1b] embryos compared with WT littermates (reduction of 51.3% in the cortical plate; Bonferroni adjusted $P < 0.0001$) (Fig. S7*J*). WDR47 is, therefore, required for proper radial migration of projection neurons.

Wdr47 Depletion Impairs Growth Cone Morphology and Microtubule Stability. Next, we turned to the investigation of fiber projections during neurodevelopment considering the extreme hypoplasia of fiber tracts in 16-wk-old mice (Fig. 3). Consistently, MRI corroborated these findings throughout the brain, showing the corpus callosum as the most affected region (Fig. 5*A*). Using the axonal (SMI-312R) and L1CAM markers to visualize neurofilaments and callosal neurons, respectively, we found fewer axonal processes both at E14.5 and E16.5 *Wdr47*[tm1b/tm1b] embryos, with thalamocortical projections unable to cross the diencephalon–telencephalon boundary (Fig. 5*B*).

Because endogenous WDR47 is expressed throughout the cytoplasm, neurites, and in the growth cone in neurons (Fig. S8*A*), we thought to assess neuronal architecture when *Wdr47* is depleted using cortical and hippocampal primary neuronal cultures at E17.5. We visualized the axon and growth cone using a marker for neurofilaments and microtubule-associated protein 2 (MAP2), a microtubule-associated protein enriched in the dendrites of neurons,
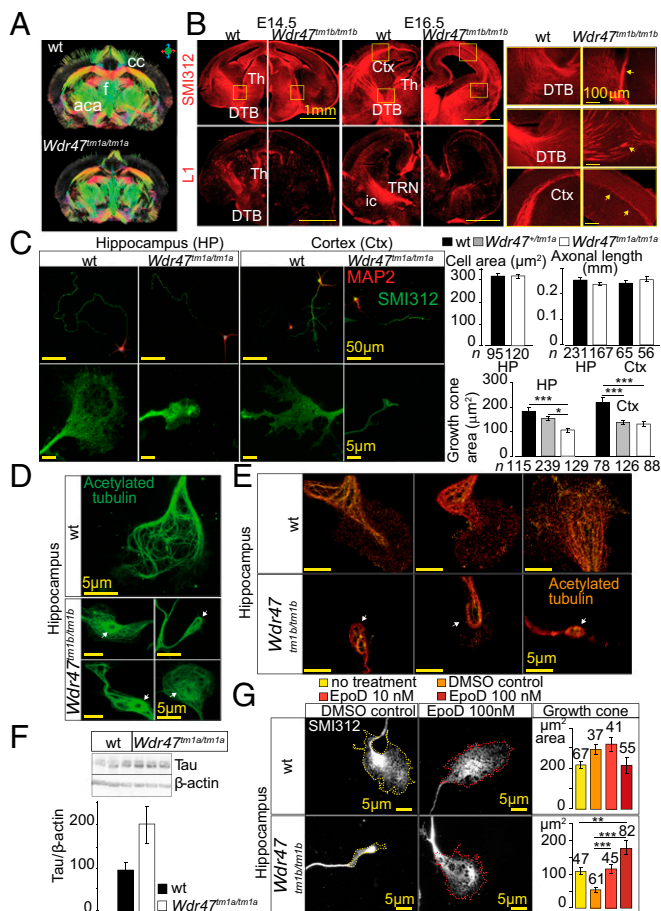
structures displayed a blunt tip and reduced filopodia protrusions, while the cell area and length of axon did not differ (Fig. 5C). These observations were confirmed in rat hypothalamic neurons treated with WDR47-specific siRNA using scanning EM (Fig. S8 B and C). In addition, time-lapse recordings from live neurons over 24 h showed that mutant growth cones are much less dynamic compared with WT (Movies S1 and S2).

The analysis of the microtubule distribution network at the growth cone of neurons derived from $Wdr47^{tm1b/tm1b}$ using acetylated tubulin as a marker of stable microtubules revealed unusual shapes, with a ring-like structure at the soma (Fig. 5D). Similar abnormalities were seen in rat hypothalamic neurons using super-resolution structured illumination microscopy; however, tubulin protein levels were not significantly altered (Fig. S8D). Super-resolution single-molecule localization microscopy also showed these unusual shapes and further established that tubulin molecules were widely dispersed in mutant as opposed to uniform and denser distribution in WT cells (Fig. 5E). Tau protein level, a microtubule-associated protein known to modulate the stability of axonal microtubules, was increased by about twofold in $Wdr47^{tm1a/tm1a}$ cortical tissue samples compared with WT (Fig. 5F). Given the role of Tau in microtubule dynamics, we hypothesized that WDR47 might participate in microtubule stabilization. We tested this by treating hippocampal primary neuronal cultures derived from $Wdr47^{tm1b/tm1b}$, characterized by a reduction of growth cone areas of -75% ($n = 162$, $P = 1.89\text{E}10^{-5}$) (Fig. 5G), with a microtubule stabilizer compound [Epothilone D (EpoD)] at two concentrations (10 and 100 nM) for 1.5 h as recommended elsewhere (26). Remarkably, EpoD was able to dose-dependently rescue growth cone size up to $+69.7\%$ relative to vehicular control (DMSO) cells (Fig. 5G). Treatment with 10 nM EpoD increased the size of growth cones by 2.1 times ($n = 102$, $P = 1.2\text{E}10^{-4}$), and treatment with 100 nM EpoD increased the size of growth cones by 3.3 times ($n = 143$, $P = 1.9\text{E}10^{-9}$). No significant changes were observed between EpoD-treated and nontreated groups in the WT. To determine whether these anomalies might be causing cell motility defects, we used a previously tested assay in neurite outgrowth (27), which relies on creating a scratch in cell culture dishes and quantifying the time required for the cells to close it (28). At 24 h postscratch introduction, the migration distance and velocity (Fig. S8E) as well as the percentage wound closing (Fig. S8F) were reduced with WDR47 siRNA treatment. All together, these results show that $Wdr47$ plays a role in stabilizing microtubules, facilitating tubulin network dynamics in both genetic mutant cells and siRNA-treated cells.

Superior Cervical Ganglion-10 Is an Interacting Partner of WDR47.

To understand the molecular mechanisms by which WDR47 might regulate microtubule stability, we next searched for interacting partners by screening a human fetal cDNA library using a yeast two-hybrid system.

Using the N terminus of WDR47 as bait, the superior cervical ganglion-10 (SCG10) protein was identified as a putative WDR47-interacting partner (Dataset S10). SCG10 is a well-established microtubule-destabilizing protein (29) regulated by JNK1, a protein kinase of the MAPK family known to phosphorylate SCG10, rendering it inactive (30). To gain insight into the mechanistic basis of this interaction, we first studied localization of WDR47, SCG10, and JNK1 in primary cortical neurons. WDR47 colocalized with SCG10 in the cytoplasm but not in the growth cone, whereas JNK1 showed colocalization with SCG10 in the cytoplasm as well as neurites (Fig. S9A). SCG10 relative mRNA expression levels showed no difference between $Wdr47^{tm1a/tm1a}$ and WT mice preparations derived from the cortex, spinal cord, thalamus, and liver (Fig. S9B). Colocalization of WDR47 and SCG10 was confirmed to occur in the cytoplasm of hypothalamic cells (Fig. S9C). Western blot analysis of endogenous SCG10 normally gives rise to four bands that range from 20 to 25 kDa, representing distinct
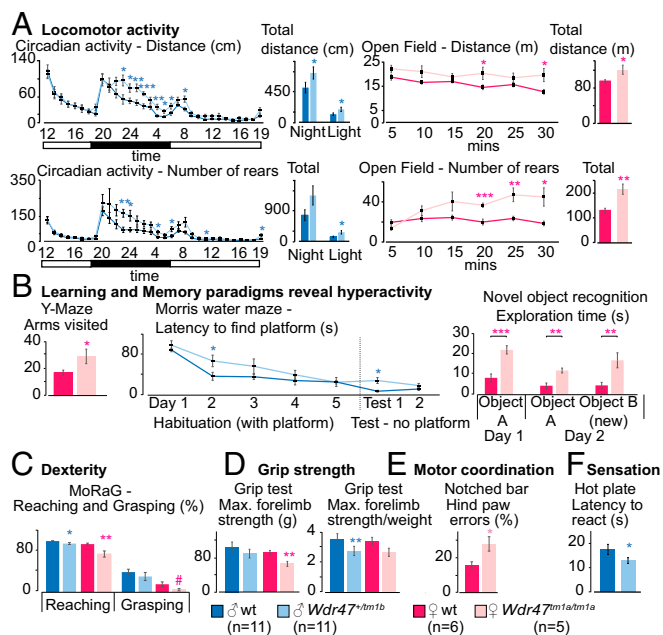
Fig. 5. Microtubule-stabilizing role of WDR47 at the growth cone. (A) MRI in $Wdr47^{tm1a/tm1a}$ male. aca, anterior part of the anterior commissure; cc, corpus callosum; f, fornix. (B) Confocal microscopy images of projection patterns in the developing brain using axonal and commissural markers at E14.5 ($n = 2$) and E16.5 ($n = 2$). Ctx, cortex; DTB, diencephalon–telencephalon barrier; ic, internal capsule; Th, thalamus; TRN, thalamic reticular nucleus. (Scale bars: Left and Center, 1 mm; and Right, 100 μm.) (C) Fluorescent microscopy images of primary neurons derived from WT and $Wdr47^{tm1a/tm1a}$ embryos at E17.5 stained with anti-MAP2 (red) and SMI-312R (green) in hippocampal (HP) and cortical (Ctx) primary neuronal cultures. Area of cell body, length of axon, and area of growth cones were quantified using ImageJ and analyzed using the Kruskal–Wallis test. (Scale bars: Upper, 50 μm; Lower, 5 μm.) (D) Microtubule architecture studied in the growth cones of hippocampal primary neurons by staining for acetylated tubulin. White arrows show odd ring-like arrangements. (E) Superresolution single-molecule localization microscopy of hippocampal growth cone stained with acetylated tubulin in $Wdr47^{tm1b/tm1b}$. (Scale bar: 5 μm.) (F) Western blot analysis of endogenous Tau levels in three $Wdr47^{tm1a/tm1a}$ compared with WT ($n = 3$). Quantification of relative protein expression is normalized against β-actin. (G) Images of primary hippocampal neurons derived from $Wdr47^{tm1b/tm1b}$ and WT embryos at E17.5 treated with 10 and 100 nM EpoD. Growth cone area was quantified using ImageJ after 1.5 h of treatment. (Scale bar: 5 μm.) ***$P < 0.001$; **$P < 0.01$; *$P < 0.05$.

and measured the area of the cell body ($n = 215$), axonal length ($n = 519$), and area of the growth cone ($n = 775$). Primary neuronal cultures derived from $Wdr47^{tm1a/tm1a}$ displayed a severe reduction of growth cone areas by 41% for the cortex ($P = 2.69\text{E}10^{-5}$) and 42% for hippocampus ($P = 1.88\text{E}10^{-6}$) (Fig. 5C), resembling the physiological collapse or catastrophe state in growth cone behavior (21). Neuronal cultures derived from $Wdr47^{+/tm1a}$ also showed smaller growth cone areas of 17% for the hippocampus ($P = 1.08\text{E}10^{-5}$) and 37% for the cortex ($P = 8.6\text{E}10^{-6}$), showing that this phenotype is also sensitive to $Wdr47$ dosage (Fig. 5C). Furthermore, these

Fig. 6. Assessment of behavioral traits in *Wdr47* mouse models. Mice were analyzed for behavioral anomalies using 16 tests (Dataset S11). Here, we show a selection of results for two cohorts: one male (11 mice *Wdr47*+/tm1b vs. 11 mice WT) and one female (5 mice *Wdr47*tm1a/tm1a vs. 7 mice WT). (*A*) Traveled distance in centimeters and numbers of rears for circadian activity recorded for 32 h and open-field activity for a duration of 30 min. (*B*) Learning and memory were tested using the Y maze (short-term memory), Morris water maze (spatial memory), and novel object recognition with retention time of 24 h (long-term memory). (*C*) Skilled movements evaluated using the MoRaG. (*D*) Grip strength for both forelimb and hind limb. (*E*) Motor coordination assessed using the notch bar. (*F*) Pain sensitivity evaluated by the latency to react to heat. All plots are represented as mean ± SEM. *P < 0.05; **P < 0.01; ***P < 0.001.

phosphorylation states (31). We assessed this in WDR47 siRNA-treated cells and quantified 22-kDa (unphosphorylated) and 25-kDa (phosphorylated) bands, but we only detected a trend for decreased 22-kDa SCG10 and increased 25-kDa SCG10 (Fig. S9*D*). Together, these results suggest that WDR47 physically interacts with the microtubule-destabilizing protein SCG10.

Wdr47 Mice Are Hyperactive and Display Sensory Motor Gating Abnormalities. To establish if the neuroanatomical defects in *Wdr47* KO mice lead to specific behavioral phenotypes, we assessed a broad range of paradigms in both male and female mice (Dataset S11 shows a list of *P* values).

The circadian activity test revealed an increase in traveled distance (*P* = 0.02) during the active phase (Fig. 6*A*). The open-field test was used to examine basic locomotor activity as well as anxiogenic behavior and showed increased total traveled distance in the arena and total number of rears (*P* = 0.001) (Fig. 6*A*) but did not show an increase in the time spent in the center, suggesting no traits of anxiety (Fig. S10*A*). The elevated plus maze test confirmed the absence of anxiogenic behavior in mice (Fig. S10*A*). Since *Wdr47* is highly expressed in the hippocampus involved in the consolidation of information, we next looked for deficits in memory using the Y-maze test to evaluate working memory, the Morris water maze for spatial memory performance, and the novel object recognition for long-term memory as well as social recognition test. Mice did not show any difficulties in learning each given task or in memorizing various objects and cues; however, they displayed, again, hyperactivity in the Y-maze (*P* = 0.04) and novel object recognition paradigms (*P* = 0.0004) (Fig. 6*B*). Because of prominent corpus callosum abnormalities, we studied forelimb

laterality and dexterity using the Mouse Reaching and Grasping (MoRaG) test (32) and found reduced reaching (*P* = 0.02 for male and *P* = 0.005 for female) abilities, while forelimb laterality was unaffected (Fig. 6*C*). Accordingly, forepaws strength was decreased as studied in a grip strength test used to assess muscular strength (Fig. 6*D*). Hind paws motor coordination was affected in the notched bar (*P* = 0.01) and gait test (Fig. 6*E*) but not ataxia (Fig. S10*B*). We also tested somatosensation using the hot plate, adhesive removal (33), and shock tests. Mice showed very significant decreased latency to react to nociceptive heat (*P* = 0.0001), indicative of increased sensitivity (Fig. 6*F*). This, however, was specific to heat stimuli, since touching sensitivity and electric shock showed no difference (Fig. S10 *C* and *D*). Finally, we tested social skills using a social interaction test but found no significant differences (Fig. S10 *E* and *F*). At the metabolic level, males developed higher (+9.7%) body weight (*P* = 0.0001) (Fig. S10*G*), despite increased hyperactivity, accounted for by increased white but not brown adipose tissue (Fig. S10*H*). Phenotypes were replicated in a validation cohort of het male mice but were milder, suggesting that the dosage sensitivity of *Wdr47* is also reflected at the behavioral level (Dataset S11). Together, these results support that the neuroanatomical defects associated with *Wdr47* KO result in hyperactivity and sensory motor gating abnormalities both in male and female mice.

To test whether behavioral phenotypes worsen with age, we generated a 56-wk-old cohort but found no difference between phenotypes detected from the same cohort at 16 wk of age, suggesting that *Wdr47* is unlikely to be implicated in neurodegeneration (Fig. S10*I*). In addition, we tested the impact of enriched diet on behavioral performances but saw no phenotypic improvement or rescue compared with mice on chow diet (Dataset S11).

WDR47 Plays a Role in Cell Homeostasis and Autophagy. Several important WDR proteins implicated in autophagy [Atg18 (34), PIK3R4 (35)] have been identified in yeast before transposition to a mammalian system. WDR47 is not normally expressed in yeast; however, this unicellular model allows us to rapidly test for a wider spectrum of biological processes. We took advantage of this to study the WDR47 C-terminal to LisH (CTLH) domain, a predicted alpha-helical sequence with function that remains completely unknown in mammals (36) (Fig. 7*A*), by overexpression of human WDR47 and LIS1 in *Saccharomyces cerevisiae* (Fig. 7*B*). While WDR47 is less expressed than LIS1 (Fig. 7*B*), delayed growth was recorded exclusively in WDR47-GFP–transformed cells (Fig. 7*C*), suggesting that WDR47 is hijacking important cellular functions. After staining of the vacuolar membrane with the lipophilic dye FM4-64 (Fig. S11*A*), we observed that LIS1-GFP was mainly cytosolic; however, on overexpression, it associated with a large punctate structure adjacent to the vacuole, whereas WDR47-GFP was associated with smaller structures in the cytoplasm (Fig. S11*A*) but not with endosomes or Golgi complex (Fig. S11*B*). These results show that, when WDR47 and LIS1 are overexpressed in yeast cells, they have different intracellular localization, and only WDR47 overexpression impairs growth.

Autophagy being essential for cell viability on nutrient starvation in yeast (37) and autophagosomes being formed at a single site next to the vacuolar membrane (38), we asked whether WDR47 or LIS1 could be localized to autophagy sites. We first used expression of WDR47 or LIS1 with mCherry-Atg8, a homolog of mammalian LC3 (39). This revealed that WDR47 impaired yeast autophagy, whereas LIS1 did not. Indeed, mCherry-Atg8 did not reach the lumen of the vacuole and accumulated into the cytoplasm (Fig. 7*D*). Coexpression of WDR47- or LIS1-GFP with mCherry-Atg8 also impaired yeast autophagy and further showed that WDR47 was associated with punctate structures that did not colocalize with Atg8 (Fig. 7*E*). These results suggest that WDR47 might interact with some yeast autophagy effector, thereby inhibiting this cellular process.

To investigate this hypothesis in mammalian cells, we tested autophagy in GT1-7 WDR47 siRNA-treated cells and quantified
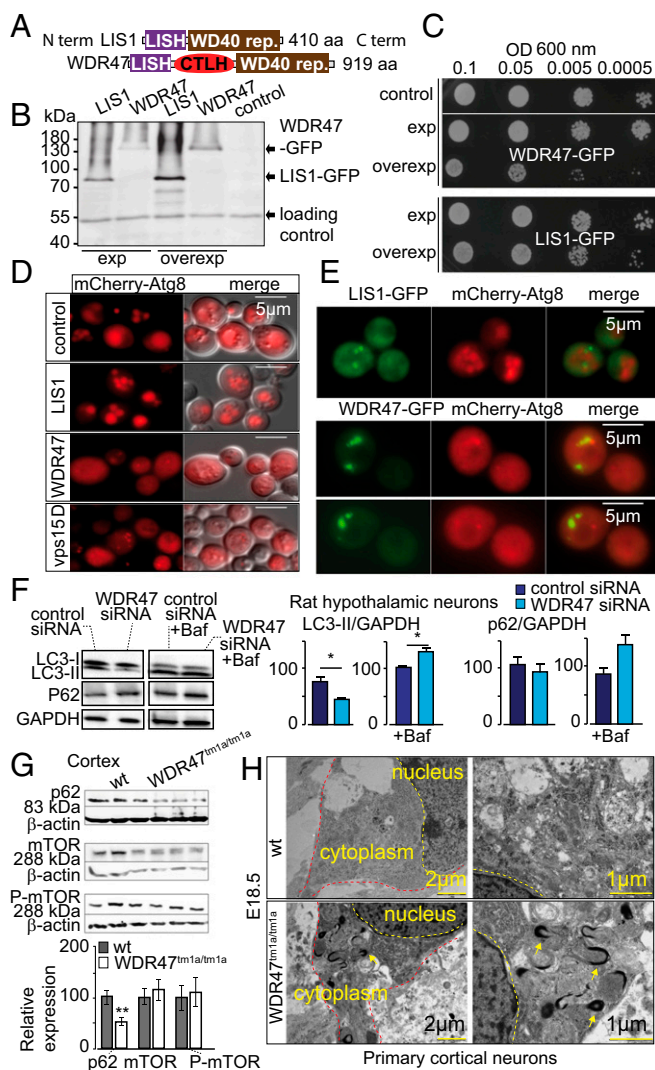
Fig. 7. WDR47 is a key effector of autophagy. (*A*) WDR47 and LIS1 structures. (*B*) Western blot on yeast protein extracts with anti-GFP antibodies. (*C*) Drop test growth assays done on WT yeast cells (BY4742) transformed with pAG413 [low-copy number centromere (CEN) plasmid; expression] or pAG423 (2 microns; over-expression) plasmids bearing LIS1 or WDR47. Midlog phase cultures of the indicated yeast cells serially diluted to the indicated OD_{600} and spotted onto synthetic medium without histidine (SC-His). Growth evaluated after 2 d of incubation at 30 °C. (*D*) WT BY4742 (control) or vps15Δ (negative control) yeast cells transformed with mCherry-Atg8 plasmid and WT BY4742 cells cotransformed with expression plasmid (pAG413) bearing LIS1 or WDR47 cDNA observed by fluorescent micros-copy after incubation for 4 h in nitrogen starvation medium (SD-N) to induce autophagy. (Scale bars: 5 μm.) (*E*) Living WT yeast cells (BY4742) expressing human LIS1-GFP or WDR47-GFP and mCherry-Atg8 observed by fluorescence microscopy after induction of autophagy by incubation in SD-N medium. (*F*) Western blot quantification of LC3 and p62 relative protein levels in the presence and absence of Bafilomycin A1 (Baf) treatment in response to WDR47 siRNA treatment. GAPDH was used as a loading control. (*G*) Western blot images of p62, mTOR, and phospho-mTOR in the cortex of WT and *Wdr47*[tm1a/tm1a]. Quantification of relative protein expression normalized against β-actin is plotted as mean ± SEM (*n* = 6 *Wdr47*[tm1a/tm1a] and *n* = 9 WT, male and female). *$P < 0.05$; **$P < 0.01$. (*H*) Transmission EM of cortical neurons from *Wdr47*[tm1a/tm1a] embryos (*n* = 3) at E18.5 compared with WT (*n* = 3). (Scale bars: *Left*, 2 μm; *Right*, 1 μm.)

levels of LC3 and p62 (or SQSTM1), two key proteins involved in autophagy. We found that LC3-II levels, but not LC3-I, were reduced (Fig. 7*F*). To assess whether this is caused by increased autophagic flux or decreased autophagosomal synthesis, we treated both WDR47 siRNA-treated and siRNA control groups with bafi-

lomycin A1, a potent inhibitor of the H$^+$ ATPase that reduces ly-sosomes functionality, and found that both LC3-II and p62 levels were increased (Fig. 7*F*), indicating enhanced autophagy flux. We also tested the expression of p62 and mTOR (an upstream regulator of autophagy) in cortices from adult *Wdr47*[tm1a/tm1a], showing a clear specificity of WDR47 function in p62-mediated autophagy (Fig. 7*G*). In addition, transmission EM revealed abnormal autophagosomes in the cytoplasm of primary neuronal cultures (Fig. 7*H*). Together, these data show an additional role of WDR47 in cell homeostasis and protein clearance by modulating autophagic activity.

Discussion

WDR proteins have recently emerged in the field of neuroscience, but their function and ultimately, their participation in shaping the mammalian brain remain to be addressed. Here, we report the anal-ysis of 26 WDR proteins in brain anatomy and focus on the functional characterization at the whole-organism level using a combination of cellular, invertebrate, and vertebrate model systems (siRNA, yeast, and KO mice) of a poorly characterized member, WDR47. WDR47 is also known as Nemitin (23), a protein sharing structural homology with LIS1, a WDR protein identified 20 y ago and associated with lissencephaly (7). Our findings highlight four important points.

First, 27% of assessed WDR genes gave rise to severe brain anomalies when inactivated in mice, showing the functional impor-tance of WDR genes in brain connectivity, particularly in the genesis of the corpus callosum, a commissure that provides higher-order neurological advantages in placental mammals. This is in line with the emerging role of WDR genes in human brain pathologies as-sociated with corpus callosum anomalies. Examples include *WDR73*, *WDR81*, *ERCC8*, and *HERC1* (40). *Herc1*$^{-/-}$ was coincidently pro-cessed in our study and showed macrocephaly and enlarged corpus callosum, reminiscent of the radiographic features of human patients with *HERC1* mutations, showing the pertinence of rodent screens for translating neuroanatomical disorders in humans.

Second, while WDR47 has previously been shown to associate with microtubules (23), we report here its implication in brain development and corpus callosum genesis. Our working model is shown in Fig. 8. In the absence of WDR47, we show that both callosal and corticofugal neurons have severe fiber tract defects and abnormally shaped growth cones in conjunction with micro-cephaly linked to the exhaustion of late cortical progenitors and the consequent decrease of neurogenesis, possibly yielding to ab-normal genesis of glial cells. Together, these could provide a molecular model underlying altered motor coordination, skilled movements, and pain sensitivity. Our work also provides insights showing that WDR47 plays a microtubule stabilizer role in the growth cone. This is further supported by the interaction between the N terminus of WDR47 and SCG10 [a very well-known mi-crotubule destabilizer promoting catastrophe at the growth cone (41)], which led us to think that WDR47 might also be a regulator of SCG10 activity in the JNK1 pathway. Interestingly, KO mouse studies of *Jnk1* (42) show high behavioral similarities (for example, motor coordination defects) compared with *Wdr47*.

Third, altered levels of LC3-II and p62 proteins, concomitantly with increased autophagy flux, suggest that WDR47, unlike LIS1, is involved in the regulation of key effectors of autophagy in the brain. Autophagy is a protein clearance process of aberrant or obsolete cellular structures and organelles crucial in cell homeo-stasis. Microtubules seem an important player in the autophagy process in mammals (43); however, their specific implication in autophagy is unclear (44). A potential molecular mechanism by which WDR47 regulates autophagy might be through its interaction with the light chain of MAP8 (also known as MAP1S) (23). In a similar way to MAP8 (45), WDR47 might bridge the autophagy machinery, in particular, LC3-II–bound autophagosomes, with microtubules. Unlike other cells of the mammalian system, postmitotic neurons are more vulnerable to damage from cellular debris and thus, would require a well-regulated degradation pathway.
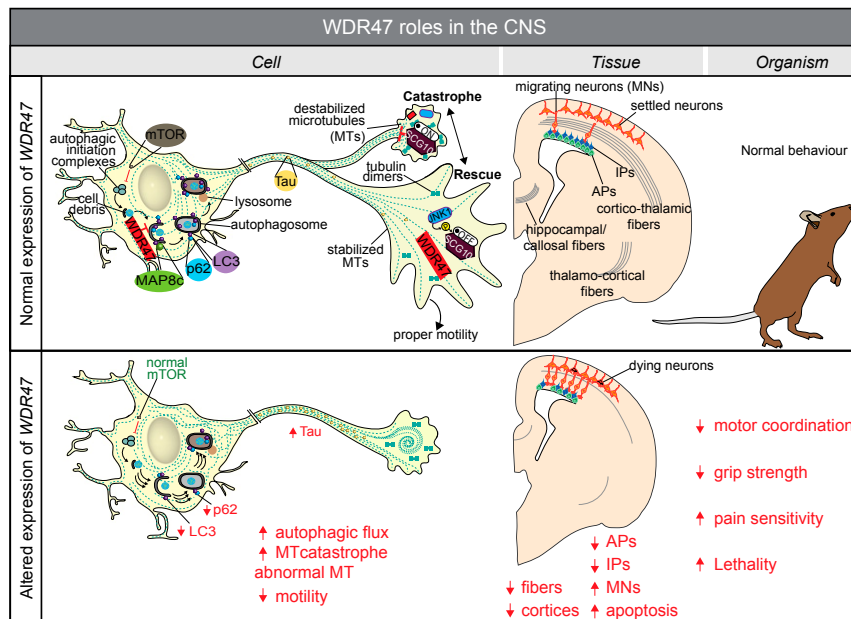
Fig. 8. Summary of WDR47 working model. At the cellular level, WDR47 acts as a stabilizer of microtubules. SCG10, a microtubule destabilizer at the growth cone, is regulated by JNK1 through phosphorylation. In the cytoplasm, WDR47 negatively regulates p62 and LC3-mediated autophagy. Reduced expression of *Wdr47* leads to destabilization of the microtubules, increased Tau and autophagic flux, and decreased cell motility. At the tissue level, the loss of *Wdr47* yields fiber tract defects, including corpus callosum agenesis, microcephaly, and thinner cortices, that are linked to a reduced number of progenitors, increased number of neurons in the intermediate zone, and elevated number of dying neurons in the cortical upper layers. At the organism level, these defects may explain impairment in motor coordination, reduced grip strength, and increased pain sensitivity. AP, apical progenitor; IP, intermediate progenitor; MN, migrating neuron; MT, microtubule.

WDR47 involvement in the survival of postmitotic neurons in late corticogenesis from upper cortical layers, where WDR47 is the most expressed, could be mediated through the proper regulation of autophagy, reinforcing the molecular cross-talk between autophagy and apoptosis (46). Furthermore, the possible association of WDR47-related autophagy to brain wiring is supported by a recent report showing that the WDR autophagy scaffold protein (ALFY) is required for neuronal connectivity in the mouse brain (47). Strikingly, the lack of *Alfy* in mice led to perinatal lethality, microcephaly, absence of the corpus callosum, and hypoplasia of the internal capsule (47), reminiscent of *Wdr47* phenotypes, suggesting a similar mode of action. It may, therefore, be that WDR47 regulates the cell ability to detect environmental cues via its microtubule stabilization role, which in turn, regulates the protein degradation pathway necessary for neuronal shape and motility.

Fourth, the final significant finding is the essential role of WDR47 for survival. The scarcity of patients harboring mutations in WDR47 supports this notion. Indeed, we found no truncating mutations in *WDR47*, despite sharing data at numerous genetic meetings, and only three stop-gained mutations are reported in the ExAC database (48), suggesting a selection bias against LoF mutations in *WDR47*. Extending our analysis to three specific cohorts of unknown genetic cause made up of patients with lissencephaly, intellectual disability, and nonsyndromic agenesis of the corpus callosum, we identified three missense variants (Datasets S12 and S13); however, pathogenicity and transmission mode were not compatible with *WDR47* gene causality. The inability of *S. cerevisiae* to grow, possibly because of the inhibition of autophagy on overexpression of WDR47, further supports the essentiality of WDR47 for survival but also suggests that mirrored protein levels (too little or too much) have identical effects on pathogenicity and underlying biological processes. This is a characteristic of scaffold proteins, indicating that WDR47 might be serving as a support for the interaction of other proteins, such as SCG10. Although we were unable to identify the precise reason of death, cardiac and breathing failure were excluded. Autophagy being dramatically up-regulated

in the neonatal stage to overcome the starvation period (49), mice could be dying of lack of nutrients, since an enriched lipid diet rescued lethality.

In conclusion, this study presents identification of the relevance of WDR genes in brain connectivity, highlighting the power of unbiased and high-throughput mouse LoF studies in the field of neuroscience. These mouse models could explain some of the missing genetics in corpus callosum biology (11) and help pave the way for a better stratification system of complex neurodevelopmental steps. WDR47 plays a role in the regulation of microtubule dynamics, progenitor proliferation, neuronal migration, and fiber tract projections in a similar fashion to LIS1 (50, 51) but with the distinctive particularity that WDR47 inhibits autophagic flux. This provides a functional link between autophagy biology and the CTLH domain (52) in mammals [this association was previously made with the vacuole import and degradation pathways in yeast (53)], while strengthening the emerging link between autophagy and microtubules assembly. Although a definite association of WDR47 with human brain disorders has not been made yet, WDR47 should be considered as a candidate gene for corpus callosum abnormalities and motor coordination deficiencies, possibly through compound heterozygosity or somatic mosaicism. Considering that the microtubule stabilizer drug restored growth cone defects, it will be interesting to test whether the behavioral anomalies, as already shown in an Alzheimer mouse model (54), could also be restored. This might open up therapeutic perspectives in the clinic with the aim of relieving symptoms in patients suffering from this class of diseases that we refer to as "WDRopathies."

Materials and Methods

Mutant mice were obtained through collaboration with the Sanger Mouse Genetics Project. *Wdr47*-targeted mice were generated using the International Mouse Phenotyping Consortium targeting mutation strategy (55). This relies on the identification of an exon common to all transcript variants, upstream of which an LacZ cassette was inserted to make a KO (tm1a), whereas tm1b creates a frameshift mutation on deletion of the selected exon. Animal procedures were approved by the local ethics committee

1. Andrade MA, Perez-Iratxeta C, Ponting CP (2001) Protein repeats: Structures, functions, and evolution. *J Struct Biol* 134:117–131.
2. Sondek J, Bohm A, Lambright DG, Hamm HE, Sigler PB (1996) Crystal structure of a G-protein beta gamma dimer at 2.1A resolution. *Nature* 379:369–374.
3. Stirnimann CU, Petsalaki E, Russell RB, Müller CW (2010) WD40 proteins propel cellular networks. *Trends Biochem Sci* 35:565–574.
4. Smith TF, Gaitatzes C, Saxena K, Neer EJ (1999) The WD repeat: A common architecture for diverse functions. *Trends Biochem Sci* 24:181–185.
5. Hurtley S (2009) Spatial cell biology. Location, location, location. Introduction. *Science* 326:1205.
6. Sasaki S, et al. (2000) A LIS1/NUDEL/cytoplasmic dynein heavy chain complex in the developing and adult nervous system. *Neuron* 28:681–696.
7. Saillour Y, et al. (2009) LIS1-related isolated lissencephaly: Spectrum of mutations and relationships with malformation severity. *Arch Neurol* 66:1007–1015.
8. Bilgüvar K, et al. (2010) Whole-exome sequencing identifies recessive WDR62 mutations in severe brain malformations. *Nature* 467:207–210.
9. Colin E, et al. (2014) Loss-of-function mutations in WDR73 are responsible for microcephaly and steroid-resistant nephrotic syndrome: Galloway-Mowat syndrome. *Am J Hum Genet* 95:637–648.
10. Lindwall C, Fothergill T, Richards LJ (2007) Commissure formation in the mammalian forebrain. *Curr Opin Neurobiol* 17:3–14.
11. Paul LK, et al. (2007) Agenesis of the corpus callosum: Genetic, developmental and functional aspects of connectivity. *Nat Rev Neurosci* 8:287–299.
12. Paul LK, Corsello C, Kennedy DP, Adolphs R (2014) Agenesis of the corpus callosum and autism: A comprehensive comparison. *Brain* 137:1813–1829.
13. Li J, et al. (2014) A comparative diffusion tensor imaging study of corpus callosum subregion integrity in bipolar disorder and schizophrenia. *Psychiatry Res* 221:58–62.
14. Balevich EC, et al. (2015) Corpus callosum size and diffusion tensor anisotropy in adolescents and adults with schizophrenia. *Psychiatry Res* 231:244–251.
15. Edwards TJ, Sherr EH, Barkovich AJ, Richards LJ (2014) Clinical, genetic and imaging findings identify new causes for corpus callosum development syndromes. *Brain* 137:1579–1613.
16. Chédotal A (2011) Further tales of the midline. *Curr Opin Neurobiol* 21:68–75.
17. Dent EW, Gupton SL, Gertler FB (2011) The growth cone cytoskeleton in axon outgrowth and guidance. *Cold Spring Harb Perspect Biol* 3:a001800.
18. Lowery LA, Van Vactor D (2009) The trip of the tip: Understanding the growth cone machinery. *Nat Rev Mol Cell Biol* 10:332–343.
19. Sapir T, Elbaum M, Reiner O (1997) Reduction of microtubule catastrophe events by LIS1, platelet-activating factor acetylhydrolase subunit. *EMBO J* 16:6977–6984.
20. Chen JF, et al. (2014) Microcephaly disease gene Wdr62 regulates mitotic progression of embryonic neural stem cells and brain size. *Nat Commun* 5:3885.
21. Kirschner MW, Mitchison T (1986) Microtubule dynamics. *Nature* 324:621.
22. Richards LJ, Plachez C, Ren T (2004) Mechanisms regulating the development of the corpus callosum and its agenesis in mouse and human. *Clin Genet* 66:276–289.
23. Wang W, et al. (2012) Nemitin, a novel Map8/Map1s interacting protein with Wd40 repeats. *PLoS One* 7:e33094.
24. Llewellyn KJ, et al. (2014) Lipid-enriched diet rescues lethality and slows down progression in a murine model of VCP-associated disease. *Hum Mol Genet* 23:1333–1344.
25. Yuan Q, et al. (2013) Folic acid supplementation changes the fate of neural progenitors in mouse embryos of hyperglycemic and diabetic pregnancy. *J Nutr Biochem* 24:1202–1212.
26. Brizuela M, et al. (2015) The microtubule-stabilizing drug Epothilone D increases axonal sprouting following transection injury in vitro. *Mol Cell Neurosci* 66:129–140.
27. Wu CL, et al. (2012) Interplay between cell migration and neurite outgrowth determines SH2B1β-enhanced neurite regeneration of differentiated PC12 cells. *PLoS One* 7:e34999.
28. Liang CC, Park AY, Guan JL (2007) In vitro scratch assay: A convenient and inexpensive method for analysis of cell migration in vitro. *Nat Protoc* 2:329–333.
29. Riederer BM, et al. (1997) Regulation of microtubule dynamics by the neuronal growth-associated protein SCG10. *Proc Natl Acad Sci USA* 94:741–745.
30. Tararuk T, et al. (2006) JNK1 phosphorylation of SCG10 determines microtubule dynamics and axodendritic length. *J Cell Biol* 173:265–277.
31. Bondallaz P, Barbier A, Soehrman S, Grenningloh G, Riederer BM (2006) The control of microtubule stability in vitro and in transfected cells by MAP1B and SCG10. *Cell Motil Cytoskeleton* 63:681–695.
32. Tucci V, et al. (2007) Reaching and grasping phenotypes in the mouse (Mus musculus): A characterization of inbred strains and mutant lines. *Neuroscience* 147:573–582.
33. Bouet V, et al. (2009) The adhesive removal test: A sensitive method to assess sensorimotor deficits in mice. *Nat Protoc* 4:1560–1564.
34. Zhang C, Zhang F (2015) The multifunctions of WD40 proteins in genome integrity and cell cycle progression. *J Genomics* 3:40–50.
35. Stoetzel C, et al. (2016) A mutation in VPS15 (PIK3R4) causes a ciliopathy and affects IFT20 release from the cis-Golgi. *Nat Commun* 7:13586.
36. Emes RD, Ponting CP (2001) A new sequence motif linking lissencephaly, Treacher Collins and oral-facial-digital type 1 syndromes, microtubule dynamics and cell migration. *Hum Mol Genet* 10:2813–2820.
37. Suzuki SW, Onodera J, Ohsumi Y (2011) Starvation induced cell death in autophagy-defective yeast mutants is caused by mitochondria dysfunction. *PLoS One* 6:e17412.
38. Shibutani ST, Yoshimori T (2014) A current perspective of autophagosome biogenesis. *Cell Res* 24:58–68.
39. Kabeya Y, et al. (2000) LC3, a mammalian homologue of yeast Apg8p, is localized in autophagosome membranes after processing. *EMBO J* 19:5720–5728.
40. Nguyen LS, et al. (2016) A nonsense variant in HERC1 is associated with intellectual disability, megalencephaly, thick corpus callosum and cerebellar atrophy. *Eur J Hum Genet* 24:455–458.
41. Grenningloh G, Soehrman S, Bondallaz P, Ruchti E, Cadas H (2004) Role of the microtubule destabilizing proteins SCG10 and stathmin in neuronal growth. *J Neurobiol* 58:60–69.
42. Komulainen E, et al. (2014) JNK1 controls dendritic field size in L2/3 and L5 of the motor cortex, constrains soma size, and influences fine motor coordination. *Front Cell Neurosci* 8:272.
43. Mackeh R, Perdiz D, Lorin S, Codogno P, Poüs C (2013) Autophagy and microtubules– New story, old players. *J Cell Sci* 126:1071–1080.
44. Monastyrska I, Rieter E, Klionsky DJ, Reggiori F (2009) Multiple roles of the cytoskeleton in autophagy. *Biol Rev Camb Philos Soc* 84:431–448.
45. Xie R, Nguyen S, McKeehan WL, Liu L (2010) Acetylated microtubules are required for fusion of autophagosomes with lysosomes. *BMC Cell Biol* 11:89.
46. Wu HJ, Pu JL, Krafft PR, Zhang JM, Chen S (2015) The molecular mechanisms between autophagy and apoptosis: Potential role in central nervous system disorders. *Cell Mol Neurobiol* 35:85–99.
47. Dragich JM, et al. (2016) Autophagy linked FYVE (Alfy/WDFY3) is required for establishing neuronal connectivity in the mammalian brain. *Elife* 5:e14810.
48. Lek M, et al.; Exome Aggregation Consortium (2016) Analysis of protein-coding genetic variation in 60,706 humans. *Nature* 536:285–291.
49. Kuma A, et al. (2004) The role of autophagy during the early neonatal starvation period. *Nature* 432:1032–1036.
50. Cahana A, et al. (2001) Targeted mutagenesis of Lis1 disrupts cortical development and LIS1 homodimerization. *Proc Natl Acad Sci USA* 98:6429–6434.
51. Dujardin DL, et al. (2003) A role for cytoplasmic dynein and LIS1 in directed cell movement. *J Cell Biol* 163:1205–1211.
52. Kobayashi N, et al. (2007) RanBPM, Muskelin, p48EMLP, p44CTLH, and the armadillo-repeat proteins ARMC8alpha and ARMC8beta are components of the CTLH complex. *Gene* 396:236–247.
53. Alibhoy AA, Giardina BJ, Dunton DD, Chiang HL (2012) Vid30 is required for the association of Vid vesicles and actin patches in the vacuole import and degradation pathway. *Autophagy* 8:29–46.
54. Zhang B, et al. (2012) The microtubule-stabilizing agent, epothilone D, reduces axonal dysfunction, neurotoxicity, cognitive deficits, and Alzheimer-like pathology in an interventional study with aged tau transgenic mice. *J Neurosci* 32:3601–3611.
55. Skarnes WC, et al. (2011) A conditional knockout resource for the genome-wide study of mouse gene function. *Nature* 474:337–342.
56. Karp NA, Melvin D, Mott RF; Sanger Mouse Genetics Project (2012) Robust and sensitive analysis of mouse knockout phenotypes. *PLoS One* 7:e52410.
57. Wahlsten D, Metten P, Crabbe JC (2003) Survey of 21 inbred mouse strains in two laboratories reveals that BTBR T/+ tf/tf has severely reduced hippocampal commissure and absent corpus callosum. *Brain Res* 971:47–54.
58. Livak KJ, Schmittgen TD (2001) Analysis of relative gene expression data using real-time quantitative PCR and the 2(-Delta C(T)) method. *Methods* 25:402–408.
59. Mikhaleva A, Kannan M, Wagner C, Yalcin B (2016) Histomorphological phenotyping of the adult mouse brain. *Curr Protoc Mouse Biol* 6:307–332.
60. Alberti S, Gitler AD, Lindquist S (2007) A suite of gateway cloning vectors for high-throughput genetic analysis in Saccharomyces cerevisiae. *Yeast* 24:913–919.
61. Gietz D, St Jean A, Woods RA, Schiestl RH (1992) Improved method for high efficiency transformation of intact yeast cells. *Nucleic Acids Res* 20:1425.
62. Romaniello R, et al. (2016) Clinical characterization, genetics, and long-term follow-up of a large cohort of patients with agenesis of the corpus callosum. *J Child Neurol* 32:60–71.
63. Redin C, et al. (2014) Efficient strategy for the molecular diagnosis of intellectual disability using targeted high-throughput sequencing. *J Med Genet* 51:724–736.